AIAA Aviation Forum and ASCEND co-located Conference Proceedings
21 - 25 July 2025, Las Vegas, Nevada
AIAA AVIATION FORUM AND ASCEND 2025

10.2514/6.2025-3216

Improving predictive performance of low-order models using bounded trigonometric closures

Vamsi Krishna Chinta*
University of Minnesota, Minneapolis, MN 55455, USA

Diganta Bhattacharjee †
University of Minnesota, Minneapolis, MN 55455, USA

Peter Seiler‡
University of Michigan, Ann Arbor, MI 48109, USA

Maziar Hemati§
University of Minnesota, Minneapolis, MN 55455, USA

Low-order models of high-dimensional systems are useful in many settings requiring prediction, analysis, and control. However, predictive fidelity in low-order models can be compromised due to the inherent truncation of higher-order modes required to construct such models, either directly from the governing equations or using data-driven techniques. Previous studies have proposed the use of quadratic and higher-order polynomial closures to account for these truncated modes without increasing the model order. While these closures have been shown to improve predictive accuracy over short time periods, the underlying models are not guaranteed to be bounded and can result in a deterioration in predictive capability over longer time horizons. In this work, we propose a trigonometric closure model that improves predictive performance over long time periods. Trigonometric closures are formed as pairs of sine and cosine functions acting on appropriately weighted state variables, enabling prediction over a wide range of frequencies as needed to model the truncated modes. We mathematically prove that introducing the proposed trigonometric closure to a stable linear model of the system dynamics guarantees long-time boundedness of the resulting model. We demonstrate the utility of the trigonometric closures for improving a low-order linear model on two test cases: (i) a transient cylinder wake, and (ii) the periodic vortex shedding of a cylinder wake. The resulting models are found to improve predictive accuracy and maintain boundedness over hundreds of convective time units.

I. Introduction

A. Motivation and Background

Physics-based models grounded in partial differential equations have been widely used to simulate and study different types of physical systems, including fluid flows. A numerical simulation that relies on discretizing the governing equations and resolves all the spatio-temporal scales is known as a full-order model (FOM). The computational cost of FOM depends on the grid's spatio-temporal resolution. For many physical systems, such as high Reynolds number (Re) turbulent flows and rocket engine combustion, the grid's spatial resolution needs to be sufficiently high and this can incur significant computational cost. FOMs may be useful to understand complex physics but may be prohibitively expensive for design optimization or flow control applications. This motivates the need for reduced-order models (ROMs) which are computationally inexpensive while being reasonably accurate to capture the dominant physics.

Many high-dimensional physical systems evolve on a low-dimensional manifold. Reduced-order modeling techniques exploit this property to build low-order models. Projection-based reduced-order models utilize a dimensionality reduction

*Postdoctoral Associate, Aerospace Engineering and Mechanics, AIAA Member, Email: chint076@umn.edu
†Postdoctoral Associate, Aerospace Engineering and Mechanics, AIAA Member, Email: dbhattac@umn.edu
‡Associate Professor, Electrical Engineering and Computer Science, AIAA Associate Fellow, Email: pseiler@umich.edu
§Associate Professor, Aerospace Engineering and Mechanics, AIAA Associate Fellow, Email: mhemati@umn.edu

technique to project the dynamics onto a low-dimensional subspace. Linear dimensionality reduction techniques—such as proper orthogonal decomposition (POD) [1]—are popular choices for this dimensionality reduction step. POD relies on projecting the high-dimensional snapshot data of observables (from simulations or experiments) onto a low-dimensional linear subspace with the basis functions computed directly from the data. A low-order model is then built that only solves the evolution equations in the low-dimensional subspace. In other words, the ROM solves for the evolution of the coefficients of the leading POD modes, while ignoring the influence of the higher-order (truncated) modes. The original system is then reconstructed by mapping the low-dimensional latent space to the high-dimensional state space. However, ROMs that rely on a linear dimensionality reduction step cannot capture non-linear manifolds and they need to be sufficiently high dimensional to capture the interaction between the modes that drive the dynamics.

Non-linear dimensionality reduction can be used to identify complex non-linear manifolds via a non-linear mapping between the high-dimensional state space to the low-dimensional subspace [2], or by decomposing the domain into several subdomains and using a local approximation for each [3–5]. Such methods typically achieve a higher compression, thereby further reducing the size of the latent dimension compared to a linear dimensionality reduction step. One popular choice for non-linear dimensionality reduction are autoencoders [6–8]. Autoencoders map a high-dimensional state space to a low-dimensional latent space via an encoder. The dynamics are evolved in this latent space and mapped back via a decoder to the high-dimensional state space. The number of parameters to train increases with the dimension of the snapshot data and hence training can become computationally expensive. In addition, generating sufficiently large snapshot datasets by solving FOM also adds to the computational cost and in some cases, such as high-Re fluid flows, the autoencoder approach can be prohibitively expensive.

Alternative approaches for constructing nonlinear manifolds have been proposed based on quadratic and high-order polynomial functions [9–12]. However, building a low-dimensional ROM using projection-based methods require truncating higher-order modes and solve for the evolution of the leading modes. The truncated higher-order modes can influence the trajectories of the leading modes and over time the predictions diverge from the true solution. Therefore, higher dimensional ROMs tend to have higher accuracy because they capture the higher-order interactions between modes, but may be prone to instability. On the other hand, low-dimensional ROMs can be more stable, but do not account for all the higher-order interactions, and hence may be less accurate. Therefore, building a ROM that is both accurate and stable is challenging. Closure models bridge this gap by accounting for the interactions, as well as creating a mapping between the leading modes and the truncated higher-order modes. This facilitates building a low-dimensional ROM without sacrificing accuracy. However, many of the above mentioned techniques do not typically address the problem of boundedness or stability and the training process need to be modified appropriately to enforce it, which can be non-trivial [13–17].

Certifying stability of a ROM could be achieved through characterizing bounds on its trajectories, which are often established via an energy-like metric and boundedness of the metric usually translates into bounded trajectories. These ideas stem naturally from well-established methods in systems theory like Lyapunov analysis and set invariance [18, 19]. In particular, the concept of trapping regions—put forward by Schlegel and Noack [13] in the context of fluid-flow modeling and analysis—has been the focus of many ROM-related studies in recent times [15, 17, 20, 21]. A trapping region—which is closely related to the concept of ultimate boundedness [18, Chapter 4]—is a compact subset of the state space that is invariant with respect to the underlying system dynamics. Thus, once a trajectory enters the trapping region, it remains in its interior for all future times, thereby guaranteeing a bounded response from the system. Schlegel and Noack [13] provided conditions for existence of such trapping regions, which was refined recently by Liao et al. [20]. Data-driven modeling methods leveraging the existence of a trapping region have also been proposed [15, 21]. Therefore, constraints ensuring existence of a trapping region could be embedded within a data-driven model synthesis routine. An approach like that would provide a pathway for building data-driven ROMs that are both accurate and guaranteed stable. Alternatively, trapping region analysis for a given ROM could provide useful insight into the long-time behavior of the underlying model.

B. Contribution

In this work, we use a data-driven approach to build a low-order projection-based model with closure. We propose a *trigonometric closure* which consists of sine-cosine pairs of different frequencies. The choice of the closure terms is based on the desired characteristics of the closure model. We show that a trigonometric closure can approximate complex manifold shapes, form an expressive basis to map the leading modes to higher-order truncated modes, and results in a ROM that is long-time bounded when integrated to a stable linear model. We develop a rigorous proof grounded in Lyapunov analysis to show the long-time boundedness of this model and also estimate the size of the trapping region.

This is in contrast to previous closure models which do not typically guarantee stability or boundedness. In addition, this method requires fewer parameters to train when compared to autoencoders and hence the data requirements and computational cost of training is also comparatively less. We demonstrate the ability of this model's expressivity and boundedness properties on two test cases: (i) a transient cylinder wake [22], and (ii) the periodic vortex shedding in the wake of a cylinder.

C. Outline

The manuscript is organized as follows: In Section II, we discuss the reason for using trigonometric closures backed by illustrative examples. In Section III, we discuss the training procedure to obtain a low-order model with trigonometric closure. This is followed by the requirements of the model for long-time boundedness and a rigorous mathematical proof for it. Specifically, we prove that when certain conditions are satisfied, the low-order model with the proposed trigonometric closure admits a trapping region. In addition, we also propose a method—rooted in convex optimization—to compute spherical estimates of that trapping region. In Section IV, we start with the method we used to generate training data for the periodic cylinder wake test case. Then, we compare and contrast a low-dimensional 4-mode linear model with and without the proposed trigonometric closure. In particular, we demonstrate the ability of the ROM with closure in boosting accuracy while being long-time bounded. This is followed by a demonstration of the proposed trapping region estimate. Finally, we provide the concluding remarks in Section V.

II. Trigonometric Closure Model: Preliminaries

In this section we discuss the strengths of using a trigonometric closure model based on the desired characteristics of a closure. The purpose of a closure model is three fold: (1) Approximation of low-dimensional manifolds on which dynamics evolve: This is a non-linear dimensionality reduction step and it has two components: (a) Closure correction: This captures the higher-order interactions of the leading modes with the truncated modes and accounts for them as a "closure correction" to the low-dimensional model, and (b) Lifting transformation: Lift the low-order model to higher dimensions by mapping the the leading modes to the truncated ones. We show via an illustrative example that this method can approximate complex manifold shapes and hence better ROM predictions. (2) Expressive basis: This goes back to the lifting transformation mentioned previously. We show via an illustrative example that the trigonometric closure serves an expressive basis to effectively map the leading modes to the truncated ones; and (3) Longtime boundedness: A closure correction is added to boost the accuracy. However, adding a closure correction term should not destabilize an existing model, especially when it is stable or marginally stable prior to implementation of the closure. We show that when the trigonometric closure is integrated to a stable linear model, the combined model is long-time bounded. In this section we discuss each of these points in detail and show that trigonometric closure models satisfy all three.

A. Approximation of low-dimensional manifold on which dynamics evolve

We use a closure modeling approach similar to Kalur et al. [23]. To summarize their method briefly, ℓ snapshots of an N dimensional system are collected. A linear $\ell-$dimensional ($\ell \ll N$) model for the evolution of the ℓ POD modes is then constructed using the Dynamic Mode Decomposition (DMD) algorithm [24] and is given by

$$\tilde{\mathbf{x}}(k+1) = \tilde{\mathbf{A}}\tilde{\mathbf{x}}(k) \tag{1}$$

where $\tilde{\mathbf{x}} \in \mathbb{R}^{\ell}$ is an ℓ-dimensional vector of POD coefficients. An r-dimensional ($r \ll \ell$) linear model, obtained by projecting the linear operator onto an $r-$dimensional subspace, is given by

$$\hat{\mathbf{x}}(k+1) = \hat{\mathbf{A}}\hat{\mathbf{x}}(k) \tag{2}$$

where $\hat{\mathbf{x}} \in \mathbb{R}^{r}$. This $r-$dimensional linear model does not account for the influence of the $\ell - r$ truncated modes on the evolution of the leading r modes and is captured via a closure model. The closure model is defined as a mapping from the leading r modes to the $\ell - r$ truncated modes and is given by

$$\tilde{\mathbf{x}} = \mathbf{\Phi}\hat{\mathbf{x}} + \overline{\mathbf{\Phi}}\,(\hat{\mathbf{x}} \otimes \hat{\mathbf{x}}) \tag{3}$$

where $\mathbf{\Phi}^{\mathrm{T}} := [\mathbf{I}_{r\times r} \quad \mathbf{0}_{r\times(\ell-r)}]$ maps the full state vector $\tilde{\mathbf{x}}$ to the r-dimensional reduced vector $\hat{\mathbf{x}}$, i.e., $\hat{\mathbf{x}} = \mathbf{\Phi}^{\mathrm{T}}\tilde{\mathbf{x}}$. Similarly, $\mathbf{\Phi}$ lifts the reduced state vector $\hat{\mathbf{x}}$ to an ℓ-dimensional vector. Using this transformation, the first r entries

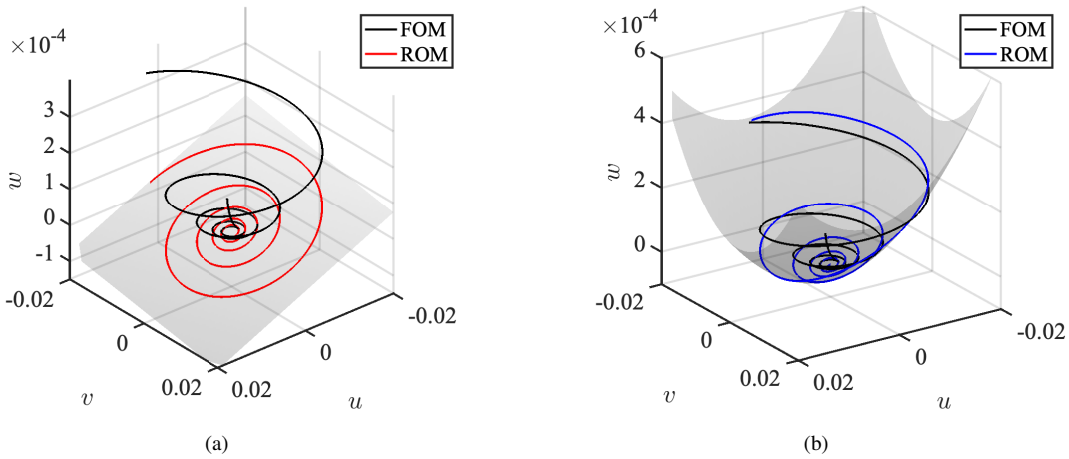

Fig. 1 Evolution of trajectories for a full-order model (FOM) (in black) and a 2 dimensional reduced-order model (ROM) (a) The trajectory of the ROM (in red), confined to a two dimensional subspace spanned by the first two POD modes. (b) Trajectory of the ROM (in blue) and the quadratic manifold it is confined to. Introducing a quadratic closure can be interpreted as projecting the FOM onto the quadratic manifold thereby reducing the projection error.

are exactly the same as $\hat{\mathbf{x}}$ and the rest are 0. $\overline{\mathbf{\Phi}} \in \mathbb{R}^{\ell \times r^2}$ is an operator mapping the leading POD coefficients ($\hat{\mathbf{x}}$) to truncated coefficients ($\tilde{\mathbf{x}} - \mathbf{\Phi}\hat{\mathbf{x}}$) via the quadratic term ($\hat{\mathbf{x}} \otimes \hat{\mathbf{x}}$). $\overline{\mathbf{\Phi}}$ is obtained via ridge regression over the training data where $\tilde{\mathbf{x}}$ (and $\hat{\mathbf{x}}$) is known. An $r-$ dimensional model with a quadratic closure is obtained by substituting Eq. (3) into Eq. (1), multiplying with $\mathbf{\Phi}^{\mathrm{T}}$ on LHS and RHS, and using the orthogonality property of $\mathbf{\Phi}^{\mathrm{T}}$ and $\overline{\mathbf{\Phi}}$ (i.e., $\mathbf{\Phi}^{\mathrm{T}}\overline{\mathbf{\Phi}} = 0$, see [11]) to obtain

$$\hat{\mathbf{x}}(k+1) = \hat{\mathbf{A}}\hat{\mathbf{x}}(k) + \hat{\mathbf{B}}\left(\hat{\mathbf{x}}(k) \otimes \hat{\mathbf{x}}(k)\right) \tag{4}$$

where $\hat{\mathbf{A}} = \mathbf{\Phi}^{\mathrm{T}}\tilde{\mathbf{A}}\mathbf{\Phi}$ and $\hat{\mathbf{B}} = \mathbf{\Phi}^{\mathrm{T}}\tilde{\mathbf{A}}\overline{\mathbf{\Phi}}$.

Kalur et al. [23] give an insightful 3D representation of this quadratic closure modeling problem. Figure 1, which has been adapted from Kalur et al. [23], shows the interpretation using a 3-dimensional visualization of the evolution of full-order and reduced-order models. The full-order model corresponds to a transient cylinder wake with the governing equations given by [22]

$$\begin{aligned} \dot{u} &= \mu u - v - uw \\ \dot{v} &= \mu v + u - vw \\ \dot{w} &= -w + u^2 + v^2 \end{aligned} \tag{5}$$

where $\mu = 1/10$. The FOM is simulated for an initial condition $\mathbf{x}_0 = (0.001, 0, 0.0001)$ with a time step $\Delta t = 0.01$ for $t = [0, 30]$. Note that these parameters are consistent with the parameter values in Kalur et al. [23] to solve the FOM and generate snapshot data.

Figure 1(a) shows the evolution of the state trajectories for a 3 dimensional full-order model in black and a 2 dimensional linear reduced-order model in red. The 2 dimensional linear model is obtained using DMD and only tracks the evolution of the first 2 POD modes, i.e., $r = 2$ in Eq.(2). Because the ROM is a linear combination of the first two POD modes, the evolution is constrained to the 2D subspace shown by the translucent plane. Figure 1(b) shows the evolution of a 2-dimensional ROM with a quadratic closure shown in Eq.(4), along with the manifold it evolves on. The truncated modes are estimated via Eq. (3) and is used to compute the evolution of the full state vector in the physical space. The effect of this quadratic closure model can be interpreted as projecting the FOM onto a quadratic manifold. Clearly, this method significantly reduces the projection error when compared to a projection onto a 2D planar surface.

Although, a quadratic closure term may boost accuracy, there is no guarantee that the combined model is stable or long-time bounded. In this work, we propose to use a trigonometric closure model with the closure terms being the

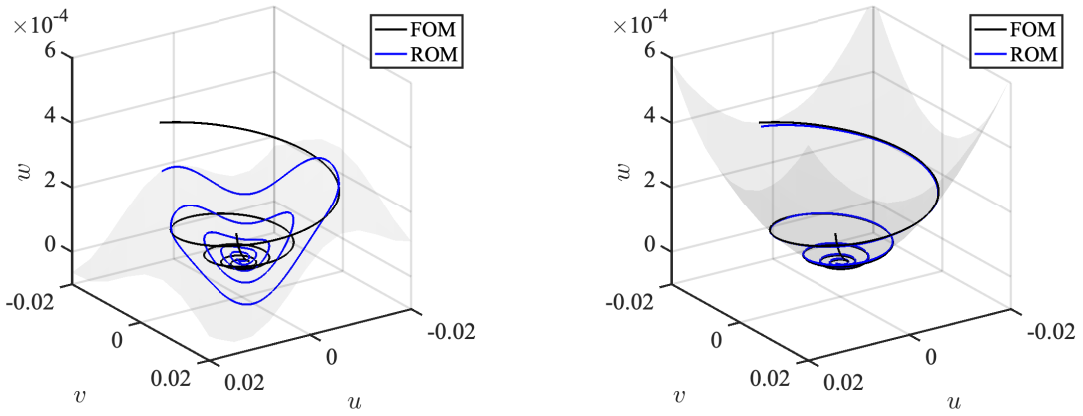

Fig. 2 Evolution of trajectories for FOM in black, and a 2 dimensional ROM with trigonometric closure in blue. (a) ROM evolution with 1 frequency per mode. The ROM does not approximate the FOM accurately and the projection error is high. (b) ROM with 2 frequencies per mode. The ROM trajectory closely approximates the FOM and the projection error is reduced. The manifold on which the FOM evolves is also better approximated as the FOM closely grazes the manifold on which the ROM evolves.

weighted sum of sine and cosine pairs of different frequencies as

$$(\tilde{\mathbf{x}} - \boldsymbol{\Phi}\hat{\mathbf{x}}) = \overline{\boldsymbol{\Phi}} \underbrace{\begin{bmatrix} \sin(2\pi f_{11} x_1) \\ \cos(2\pi f_{11} x_1) \\ \sin(2\pi f_{12} x_1) \\ \cos(2\pi f_{12} x_1) \\ \vdots \\ \sin(2\pi f_{1n} x_1) \\ \cos(2\pi f_{1n} x_1) \\ \vdots \\ \sin(2\pi f_{rn} x_r) \\ \cos(2\pi f_{rn} x_r) \end{bmatrix}}_{\tau(f_{ij}, \hat{\mathbf{x}})} \tag{6}$$

where n is the number of frequencies per state. Notice that this model is obtained by replacing the Kronecker product in Eq. (3) with the sine-cosine pairs. Therefore, it results in a different size of $\overline{\boldsymbol{\Phi}} \in \mathbb{R}^{l \times 2rn}$ compared to the quadratic closure. The number of frequencies to use is a hyperparameter and is tuned to increase the predictive fidelity.

A trigonometric closure model can be interpreted as a simplification of the Fourier series of a general $r-$ dimensional manifold without the non-linear combination of sine-cosine terms. In other words, we consider the subset of terms where the sine or cosine terms have a non-zero wavenumber for one of the state variables and the wavenumbers for other state variables are zero. Although this simplification is adhoc and not rigorously justified, it allows modeling with limited number of terms. After this simplification, the closure vector has a constant norm anywhere in the state space — an important property that we exploit for establishing global boundedness of the proposed method. We test this closure model on the same test case as before to compare and contrast with the previous quadratic closure modeling from Kalur et al. [23].

The $r-$dimensional model with a trigonometric closure model can be expressed as

$$\hat{\mathbf{x}}(k+1) = \hat{\mathbf{A}}\hat{\mathbf{x}}(k) + \hat{\mathbf{B}}\tau\left(f_{ij}, \hat{\mathbf{x}}(k)\right) \tag{7}$$

which is obtained by substituting Eq. (6) into Eq. (1), multiplying with $\mathbf{\Phi}^{\mathrm{T}}$ on LHS and RHS, and using the properties $\hat{\mathbf{x}} = \mathbf{\Phi}^{\mathrm{T}}\tilde{\mathbf{x}}, \mathbf{\Phi}^{\mathrm{T}}\overline{\mathbf{\Phi}} = 0$. Here $\hat{\mathbf{A}} = \mathbf{\Phi}^{\mathrm{T}}\tilde{\mathbf{A}}\mathbf{\Phi}$ and $\hat{\mathbf{B}} = \mathbf{\Phi}^{\mathrm{T}}\tilde{\mathbf{A}}\overline{\mathbf{\Phi}}$. We use a data-driven method to compute the frequencies f_{ij} and operators $\overline{\mathbf{\Phi}}$—the details of this training process are given in Section III.A. As before, this closure modeling approach can be interpreted as a projection of the FOM on to a manifold constructed with non-linear terms, which are the sine and cosine pairs in this case. Figure 2(a) and 2(b) show the manifold created by using 1 and 2 frequencies per state respectively. The evolution of the full order model is shown in black and that of the ROM is shown in blue. Table 1 compares an integrated error metric, employed for both quadratic and trigonometric closure models, and computed using

$$\epsilon = \frac{\|\mathbf{D} - \hat{\mathbf{D}}\|_{\mathrm{Fro}}}{\|\mathbf{D}\|_{\mathrm{Fro}}} \times 100$$

where $\|(\cdot)\|_{\mathrm{Fro}}$ is the Frobenius norm and

$$\mathbf{D} = \begin{bmatrix} u(1) & u(2) & \cdots & u(t) \\ v(1) & v(2) & \cdots & v(t) \\ w(1) & w(2) & \cdots & w(t) \end{bmatrix}, \quad \hat{\mathbf{D}} = \begin{bmatrix} \hat{u}(1) & \hat{u}(2) & \cdots & \hat{u}(t) \\ \hat{v}(1) & \hat{v}(2) & \cdots & \hat{v}(t) \\ \hat{w}(1) & \hat{w}(2) & \cdots & \hat{w}(t) \end{bmatrix}.$$

Here (u, v, w) are the state variables of the FOM and $(\hat{u}, \hat{v}, \hat{w})$ are for the estimates from the ROM. The integrated error metric shows how each of the models perform over the time horizon. Clearly, the projection error when using 2 frequencies per state is much less than using 1 frequency per state, and the manifold on which the ROM evolves also closely grazes the FOM evolution. This model also has the least error overall, even lower than the quadratic closure model. Therefore, the number of frequencies to use can be a hyperparameter to approximate complex manifold shapes by providing additional degrees of freedom to the model.

Table 1 Prediction error for quadratic and trigonometric closure models.

Case	ϵ (%)
Linear Projection	2.41
Quadratic closure	0.62
Trigonometric closure – 1 frequency/mode	0.54
Trigonometric closure – 2 frequencies/mode	0.4387

B. Expressive basis

A linear dimensionality reduction step expands the snapshot data as a linear sum of weighted basis functions. When using proper orthogonal decomposition for dimensionality reduction, the modes are ranked by their singular values, and therefore leading POD modes have higher energy. The weights (or temporal coefficients) may have different spectral content. In many cases, coefficients of the leading POD modes are narrow banded and contain low frequency content, while those of higher-order modes contain higher frequency content and are more broadbanded. Because, a closure model acts as a surrogate for the truncated modes, it should be capable of generating higher and a broadbanded frequency content from the leading modes. As we show later, this is achieved by tuning the weights f_{ij} in Eq. 6.

Consider the temporal signal $x = \sin(2\pi 10t)$, a pure-tone sinusoid of frequency 10 and its weighted sinusoidal activation $y = \sin(2\pi wx)$ where w denotes the weighting parameter. These are shown in Fig. 3. The left hand side shows the base signal x in red solid line and the derived signal y in dashed blue line. The right hand side shows the Fourier transform. The vertical red lines show the frequency of the base signal in the Fourier space. The filled blue circles correspond to the frequencies of the derived signal y. Notice that when the weight is small (see Figs. 3(a) - (b) for $w = 0.1$), the base signal and the derived signal have approximately the same frequency content. However, when the weight w is increased (see Figs. 3(c) - (d) for $w = 0.5$ and Figs. 3(e) - (f) for $w = 1$), the derived signal y becomes more broad banded with higher frequency content. This is the property we exploit to model the truncated higher-order terms as a function of the leading modes. We show later in Section IV that the first 4 leading modes of a cylinder wake can reasonably represent up to 30 truncated modes.

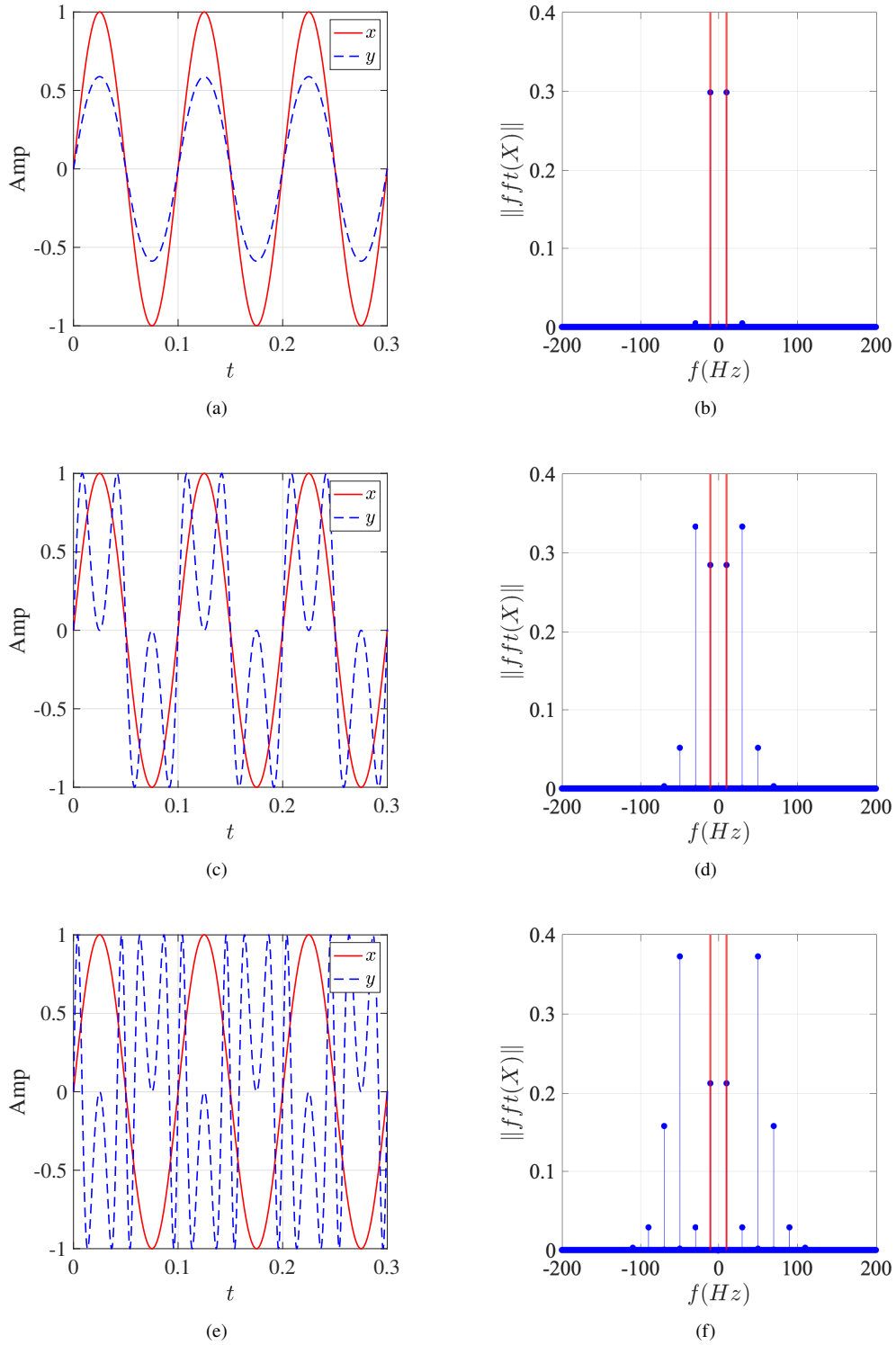

Fig. 3 Base signal x and the derived signal y obtained by sine activation of x after multiplying with a weight $2\pi w$. The plot on the left hand side show the signal in time domain while the figures on the right hand side shows the signal in frequency domain. When the weight is small ≈ 0.1, the derived signal has the same frequency content as that of the base signal. When the weight is increased, the derived signal has higher frequency content and is also more broad banded. The red vertical lines show the frequency of corresponding to the base signal x.

C. Long-time boundedness

Although closure models improve the accuracy of a low-order model [11, 12, 25], they typically do not guarantee stability of the combined model. In Section III.B, we show that when the proposed trigonometric closure model is used in conjunction with a stable linear model, the combined model admits a trapping region making the evolution long-time bounded. To summarize, the main result establishes global boundedness of the ROM with the proposed closure model by utilizing the fact that the norm of the closure terms is a constant at any point in the state space. This is in contrast to a polynomial closure model and an analysis similar to the one presented here could only lead to a local guarantee on the boundedness. A stable linear operator with spectral radius strictly less than 1 contributes towards energy dissipation. The closure terms are energy dissipative or energy producing depending on the closure operator and current state. The proof shows that outside an ellipsoidal ball, the energy is strictly decreasing. Therefore, trajectories outside this ball will eventually converge into the ball. Within the ball there can be energy production or dissipation, but the trajectories are confined within the ball. This stability property is particularly important when modeling physical systems that are bounded.

III. Low-order Model with Trigonometric Closure: Synthesis and Stability

In this section, we describe the methodology for synthesizing a low-order model with the trigonometric closure and computing the training parameters from data. This is followed by conditions and a mathematical proof, showing that the combined model admits a trapping region, and is therefore long-time bounded. This is followed by a methodology to estimate the size of the trapping region.

A. Low-order model synthesis

In this work, we test the trigonometric closure for ROMs obtained from a high dimensional linear model. We compute the linear model using the standard Dynamic Mode Decomposition (DMD) algorithm [24]. Note that the proposed method is not restricted to DMD and is suitable to other techniques for computing the linear model, including models derived as linearizations of governing equations. A brief overview of the DMD algorithm is provided here for completeness. We start by collecting the snapshots of the observables at equal time intervals and compile a data matrix $\mathbf{S}$. A new data matrix $\mathbf{S}'$ is compiled by time shifting the snapshots one step ahead in time. These matrices are given by

$$\mathbf{S} = \begin{bmatrix} | & | & & | \\ \mathbf{s}_1 & \mathbf{s}_2 & \cdots & \mathbf{s}_{\ell-1} \\ | & | & & | \end{bmatrix}, \qquad \mathbf{S}' = \begin{bmatrix} | & | & & | \\ \mathbf{s}_2 & \mathbf{s}_3 & \cdots & \mathbf{s}_{\ell} \\ | & | & & | \end{bmatrix}. \tag{8}$$

The POD modes ($\mathbf{U}$) and their coefficients ($\mathbf{\Sigma V}^{\mathrm{T}}$) are computed after a singular value decomposition of the data matrix $\mathbf{S}$. If the number of snapshots used (ℓ) is less than the dimension of the observables (N) ($\ell \ll N$), then a rank-ℓ approximation can be made without any loss of information. In other words, because the rank of the data matrix is ℓ, the reconstruction will be exact after trimming down the $\mathbf{\Sigma}$ matrix to be a square and neglecting the columns of $\mathbf{U}$ greater than ℓ. This rank-ℓ truncation is given by

$$\mathbf{S} = \mathbf{U\Sigma V}^{\mathrm{T}} = \mathbf{U}_\ell \mathbf{\Sigma}_\ell \mathbf{V}_\ell^{\mathrm{T}}. \tag{9}$$

A linear model for the evolution of these POD coefficients ($\tilde{\mathbf{x}} = \mathbf{\Sigma}_\ell \mathbf{V}_\ell^{\mathrm{T}}$) is built using the standard DMD approach. This model will have the form given in Eq. (1), where $\tilde{\mathbf{A}} = \mathbf{U}^{\mathrm{T}}\mathbf{S}'\mathbf{V}_\ell\mathbf{\Sigma}^{-1}$. To build a low-order model of dimension r, this high dimensional operator is projected on to an r-dimensional space $\hat{\mathbf{A}} = \mathbf{\Phi}^{\mathrm{T}}\tilde{\mathbf{A}}\mathbf{\Phi}$, where $\mathbf{\Phi}$ and $\mathbf{\Phi}^{\mathrm{T}}$ are defined in Section II.A. Then the r-dimensional reduced-order model will have form given in Eq. (2). Typically, for low-order models $r \ll \ell$. The evolution of the r-dimensional state trajectories $\hat{\mathbf{x}}$ given by the above model may not be accurate because the higher-order interactions are not accounted for. Furthermore, a low-rank reconstruction of the high-dimensional state will have higher error in general. Therefore a closure model should be able to account for: 1) Closure correction: This accounts for the interaction of the truncated modes with the retained or leading modes and corrects their solution trajectories. 2) Lifting transformation: Estimation of truncated modes (or higher-order modes) from the leading (retained) modes. These truncated modes were previously estimated a quadratic closure term [11, 23] i.e., using a Kronecker product of the reduced state vectors, see Eq. (3). With the proposed closure model, the quadratic term ($\hat{\mathbf{x}} \otimes \hat{\mathbf{x}}$) is replaced with the trigonometric terms as shown in Eq. (6). The reduced-order model with the

trigonometric closure is obtained by substituting Eq. (6) into the $\ell-$ dimensional linear model in Eq. (1), multiplying with $\mathbf{\Phi}^{\mathrm{T}}$ on LHS and RHS, and using the properties $\hat{\mathbf{x}} = \mathbf{\Phi}^{\mathrm{T}}\tilde{\mathbf{x}}$, $\mathbf{\Phi}^{\mathrm{T}}\overline{\mathbf{\Phi}} = 0$ to obtain Eq. (7). The operators of the resulting ROM are given by $\hat{\mathbf{A}} = \mathbf{\Phi}^{\mathrm{T}}\tilde{\mathbf{A}}\mathbf{\Phi}$ and $\hat{\mathbf{B}} = \mathbf{\Phi}^{\mathrm{T}}\tilde{\mathbf{A}}\overline{\mathbf{\Phi}}$

The number of frequencies to choose per mode is a hyperparameter to tune and we showed the influence of number of frequencies on the accuracy of the ROM in Fig. 2. A two-step procedure is used to compute the frequencies f_{ij} and the closure operator $\overline{\mathbf{\Phi}}$. The loss function for this problem is defined as

$$\mathcal{L} = \| \left(\tilde{\mathbf{x}} - \mathbf{\Phi}\hat{\mathbf{x}}\right) - \overline{\mathbf{\Phi}}\tau\left(f_{ij}, \hat{\mathbf{x}}\right) \| \tag{10}$$

where $\tau\left(f_{ij}, \hat{\mathbf{x}}\right)$ is as shown in Eq. (6). The two step process implemented in this work is summarized in Algorithm 1, wherein we use the 'MultiStart' optimization routine in MATLAB to solve for the frequencies.

Algorithm 1 Procedure for computing frequencies (f_{ij}) and closure operator ($\overline{\mathbf{\Phi}}$)

Input: $\tilde{\mathbf{x}}$, $\hat{\mathbf{x}}$, $\mathbf{\Phi}$, $\mathcal{L}_{min}$
Output: f_{ij}, $\overline{\mathbf{\Phi}}$
Initialize the frequencies f_{ij} from a random distribution
Compile the LHS $\left(\tilde{\mathbf{x}} - \mathbf{\Phi}\hat{\mathbf{x}}\right)$ and RHS $\left(\tau\left(f_{ij}, \hat{\mathbf{x}}\right)\right)$ matrices of the closure formulation in Eq. (6) over the trainig data
while $\mathcal{L} > \mathcal{L}_{min}$ **do**
Step 1: Freeze f_{ij} and compute $\overline{\mathbf{\Phi}}$ using ridge regression
Step 2: Freeze $\overline{\mathbf{\Phi}}$ and solve an optimization step to minimize the loss function $\mathcal{L}$ in Eq. (10) and update f_{ij}
end while

Note that Algorithm 1 involves optimizing over the frequencies f_{ij} in the closure model, and the number of frequencies to train using this approach is rn. Taking an alternative approach, the closure operator $\overline{\mathbf{\Phi}} \in \mathbb{R}^{\ell \times 2rn}$ and frequencies f_{ij} can be computed simultaneously by minimizing the loss function in Eq. (10). In such a formulation, the number of parameters to train/optimize would equal to $2(\ell - r)rn + rn$, which could be significantly higher than the two-step approach outlined in Algorithm 1 and might require significantly more computational resources. Furthermore, the two-step approach significantly enhances the accuracy of the solution, although results are not shown here for brevity.

B. Trapping Region Characterization

The trigonometric closure modeling with a stable linear model admits a trapping region, which ensures long-time boundedness of the combined model. We start by stating the technical assumptions for the ensuing analysis.

Assumption 1 *The governing system* (7) *satisfies the following:*
1) The matrix $\hat{\mathbf{A}}$ *is stable, i.e.,* $\rho(\hat{\mathbf{A}}) < 1$ *where* $\rho(\cdot)$ *denotes the spectral radius.*
2) The closure vector is unit norm, i.e., $\|\tau(f_{ij}, \hat{\mathbf{x}}(k))\| = 1$ *for all* $\hat{\mathbf{x}}(k)$.

Note that the unit norm assumption here is without loss of generality as the norm of the closure vector can be absorbed into the operator $\hat{\mathbf{B}}$. Assumption 1 ensures asymptotic stability of discrete-time linear dynamics for use with DMD. A continuous-time formulation can be derived using the appropriate stability conditions. Next, we provide the definition of a trapping region.

Definition 1 ([13, 20]) *A trapping region is compact set that is forward invariant with respect to the governing system. Thus, once a trajectory enters the trapping region, it remains in the trapping region for all future times. A trapping region is termed globally monotonically attracting if an energy function is strictly monotonically decreasing along all trajectories starting from an arbitrary state outside of the trapping region.*

Note that the discussion here will focus on monotonically attracting trapping regions, but we will use the term "trapping regions" for simplicity. The trapping region could be characterized using an ellipsoid and the approach outlined here is conceptually similar to the region of attraction characterization in [26, 27]. An alternative characterization is provided in Appendix A. The main technical result related to the ellipsoidal approach is summarized next, wherein $\mathbf{I}$ and $\mathbf{O}$ respectively denote identity and null matrices of appropriate dimensions.

Theorem 1 *Under Assumption 1, if there exists* $\mathbf{P} > 0$, $\lambda_1 \geq 0$ *and* $\lambda_2 \in \mathbb{R}$ *such that*

$$\begin{bmatrix} \hat{\mathbf{A}}^{\mathrm{T}}\mathbf{P}\hat{\mathbf{A}} - \mathbf{P} & \hat{\mathbf{A}}^{\mathrm{T}}\mathbf{P}\hat{\mathbf{B}} & \mathbf{O} \\ \hat{\mathbf{B}}^{\mathrm{T}}\mathbf{P}\hat{\mathbf{A}} & \hat{\mathbf{B}}^{\mathrm{T}}\mathbf{P}\hat{\mathbf{B}} & \mathbf{O} \\ \mathbf{O} & \mathbf{O} & 0 \end{bmatrix} + \lambda_1 \begin{bmatrix} \mathbf{P} & \mathbf{O} & \mathbf{O} \\ \mathbf{O} & \mathbf{O} & \mathbf{O} \\ \mathbf{O} & \mathbf{O} & -1 \end{bmatrix} + \lambda_2 \begin{bmatrix} \mathbf{O} & \mathbf{O} & \mathbf{O} \\ \mathbf{O} & -\mathbf{I} & \mathbf{O} \\ \mathbf{O} & \mathbf{O} & 1 \end{bmatrix} < 0 \tag{11}$$

then $\{\hat{\mathbf{x}} \in \mathbb{R}^r : \hat{\mathbf{x}}^{\mathrm{T}}\mathbf{P}\hat{\mathbf{x}} \leq 1\}$ *is a trapping region for system* (7).

Proof: Consider a generalized (quadratic) energy function given by $V(\hat{\mathbf{x}}(k)) = \hat{\mathbf{x}}^{\mathrm{T}}(k)\mathbf{P}\hat{\mathbf{x}}(k)$ where $\mathbf{P} > 0$ and set $\tau(k) := \tau(f_{ij}, \hat{\mathbf{x}}(k))$ to simplify notations. Now, multiply (11) on the left by $\begin{bmatrix} \hat{\mathbf{x}}^{\mathrm{T}}(k) & \tau^{\mathrm{T}}(k) & 1 \end{bmatrix}$ and on the right by $\begin{bmatrix} \hat{\mathbf{x}}^{\mathrm{T}}(k) & \tau^{\mathrm{T}}(k) & 1 \end{bmatrix}^{\mathrm{T}}$ to obtain

$$V(\hat{\mathbf{x}}(k+1)) - V(\hat{\mathbf{x}}(k)) + \lambda_1(V(\hat{\mathbf{x}}(k)) - 1) + \lambda_2\left(1 - \|\tau(k)\|^2\right) < 0. \tag{12}$$

The last term on the left hand side of the above inequality (12) is zero under Assumption 1. Also, for $V(\mathbf{x}(k)) \geq 1$, we have $V(\hat{\mathbf{x}}(k+1)) - V(\hat{\mathbf{x}}(k)) < 0$ from (12) as $\lambda_1 \geq 0$. Thus, energy decreases in the region characterizing $V(\hat{\mathbf{x}}) \geq 1$, which is the set $\{\hat{\mathbf{x}} \in \mathbb{R}^r : \hat{\mathbf{x}}^{\mathrm{T}}\mathbf{P}\hat{\mathbf{x}} \geq 1\}$. Note that a $\lambda_1 \geq 0$ satisfying (11) would mean $\hat{\mathbf{A}}^{\mathrm{T}}\mathbf{P}\hat{\mathbf{A}} - \mathbf{P} + \lambda_1\mathbf{P} < 0$ or $\lambda_1\mathbf{P} < \mathbf{P} - \hat{\mathbf{A}}^{\mathrm{T}}\mathbf{P}\hat{\mathbf{A}} \leq \mathbf{P}$ which yields $\lambda_1 < 1$. Now, setting $\lambda_3 = 1 - \lambda_1$ and rewriting (12) in terms of λ_3 gives

$$V(\hat{\mathbf{x}}(k+1)) - 1 + \lambda_3(-V(\hat{\mathbf{x}}(k)) + 1) + \lambda_2\left(1 - \|\tau(k)\|^2\right) < 0$$

which implies that $V(\hat{\mathbf{x}}(k+1)) < 1$ whenever $V(\hat{\mathbf{x}}(k)) < 1$ as $\lambda_3 > 0$ and $\left(1 - \|\tau(k)\|^2\right) = 0$ under Assumption 1. Therefore, the sub-level set $\{\hat{\mathbf{x}} \in \mathbb{R}^r : V(\hat{\mathbf{x}}) \leq 1\}$ or $\{\hat{\mathbf{x}} \in \mathbb{R}^r : \hat{\mathbf{x}}^{\mathrm{T}}\mathbf{P}\hat{\mathbf{x}} \leq 1\}$ is a trapping region of system (7). □

The trapping region characterized above is an ellipsoid which can be outer bounded using a norm ball of radius R. In other words, we require $\{\hat{\mathbf{x}} \in \mathbb{R}^r : \hat{\mathbf{x}}^{\mathrm{T}}\mathbf{P}\hat{\mathbf{x}} \leq 1\} \subseteq \{\hat{\mathbf{x}} \in \mathbb{R}^r : \hat{\mathbf{x}}^{\mathrm{T}}\hat{\mathbf{x}} \leq R^2\}$, which can be enforced through the following set-containment result:

Lemma 1 *If there exists* $\lambda_4 \geq 0$ *such that*

$$\begin{bmatrix} \lambda_4\mathbf{P} - \mathbf{I} & \mathbf{O} \\ \mathbf{O} & R^2 - \lambda_4 \end{bmatrix} \geq 0, \tag{13}$$

then $\{\hat{\mathbf{x}} \in \mathbb{R}^r : \hat{\mathbf{x}}^{\mathrm{T}}\mathbf{P}\hat{\mathbf{x}} \leq 1\} \subseteq \{\hat{\mathbf{x}} \in \mathbb{R}^r : \hat{\mathbf{x}}^{\mathrm{T}}\hat{\mathbf{x}} \leq R^2\}$.

Proof: The set-containment condition dictates that all $\hat{\mathbf{x}}$ satisfying $\hat{\mathbf{x}}^{\mathrm{T}}\mathbf{P}\hat{\mathbf{x}} \leq 1$ imply $\hat{\mathbf{x}}^{\mathrm{T}}\hat{\mathbf{x}} \leq R^2$. Using the S-procedure, this is equivalent to finding a $\lambda_4 \geq 0$ such that $\hat{\mathbf{x}}^{\mathrm{T}}\hat{\mathbf{x}} - R^2 \leq \lambda_4(\hat{\mathbf{x}}^{\mathrm{T}}\mathbf{P}\hat{\mathbf{x}} - 1)$ which can be expressed as

$$\begin{bmatrix} \hat{\mathbf{x}} \\ 1 \end{bmatrix}^{\mathrm{T}} \begin{bmatrix} \mathbf{I} - \lambda_4\mathbf{P} & \mathbf{O} \\ \mathbf{O} & \lambda_4 - R^2 \end{bmatrix} \begin{bmatrix} \hat{\mathbf{x}} \\ 1 \end{bmatrix} \leq 0 \Rightarrow \begin{bmatrix} \lambda_4\mathbf{P} - \mathbf{I} & \mathbf{O} \\ \mathbf{O} & R^2 - \lambda_4 \end{bmatrix} \geq 0.$$

This completes the proof. □

This result is a necessary and sufficient condition for set-containment as we have used the lossless S-procedure (see, e.g., [28, 29] for details). We can optimize over the radius R to find the smallest ball containing the ellipsoidal trapping region as

$$\begin{aligned} &\min_{\mathbf{P}>0, \lambda_1 \geq 0, \lambda_2, \lambda_4 \geq 0, R^2} R^2 \\ &\text{subject to (11), (13).} \end{aligned} \tag{14}$$

However, the constraints (11) and (13) are non-convex (or bilinear) due to the terms $\lambda_1\mathbf{P}$ and $\lambda_4\mathbf{P}$, respectively. Note that (13) requires $R^2 - \lambda_4 \geq 0$ with a $\lambda_4 \geq 0$. Thus, the minimum radius R satisfies $R^2 = \lambda_4$ and the set containment condition becomes $R^2\mathbf{P} \geq \mathbf{I}$. Define $\gamma := 1/R^2$ and the optimization (14) can be reformulated as

$$\begin{aligned} &\max_{\mathbf{P}>0, \lambda_1 \geq 0, \lambda_2, \gamma} \gamma \\ &\text{subject to (11), } \mathbf{P} \geq \gamma\mathbf{I} \end{aligned} \tag{15}$$

where the non-convex constraint (13) is replaced with $\mathbf{P} \geq \gamma \mathbf{I}$ which is convex. However, (15) is not a convex program due to the bilinear term $\lambda_1 \mathbf{P}$ in the constraint (11). As such, we grid over λ_1 and obtain a semi-definite program involving linear matrix inequalities for each λ_1 on the grid (see Section IV.B).

IV. Numerical results

In this section we show results corresponding to two test cases: (i) a periodic cylinder wake, and (ii) a two-dimensional limit cycle. In the first test case we show that a low-dimensional stable linear model with the trigonometric closure can accurately predict the evolution of the FOM well beyond the training snapshots. This test case showcases the advantages of using the proposed trigonometric closure in building low-order model for high-dimensional system without sacrificing accuracy and ensuring stability. For the second test case, we plot the trajectories of a two dimensional limit cycle to visualize the trapping region. We then compute it's radius using the method discussed in section III.B and compare it with the radius from the plot to demonstrate it's effectiveness.

A. Periodic vortex shedding in a cylinder wake

The test case we consider here is the periodic vortex shedding in the wake of a cylinder. We use the immersed boundary projection method (IBPM) [30, 31] available online in the github repository [32] to solve the FOM and obtain the velocity field snapshots for a cylinder wake at $Re = 100$. The simulation is run sufficiently long to let the transients evolve into a periodic vortex shedding. A total of 475 snapshots are obtained with equal time spacing which represent about 16 vortex shedding cycles. Of these 152 snapshots are used for training and the rest are used for testing.

This system is known to be long-time bounded, i.e., the solution trajectories remain bounded regardless of how long it is run or observed. Although POD does not separate out modes by its frequency content, the leading POD coefficients of a cylinder wake have a narrow-banded and low frequency content while the higher-order POD coefficients have higher and broad-banded frequency content. Therefore this particular test case demonstrates the expressivity of the closure basis, and the long-time boundedness of the resulting low-order model.

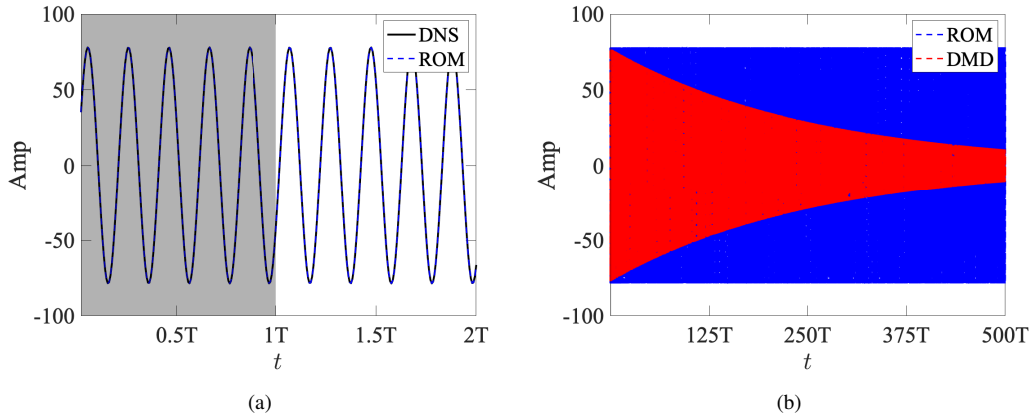

Fig. 4 Time evolution of the second POD mode for different time horizons (a) Comparison between DNS and ROM (b) Comparison between a 4-mode DMD without closure and the ROM. Here we refer to DMD with trigonometric closure as the ROM and T stands for the training time horizon.

We compare the results from the trigonometric closure modeling approach proposed in this work against the standard DMD test case. For this test case, the ROM is built using 4-dimensional linear operator with trigonometric closure with 8 frequencies per mode. The linear operator is obtained via DMD, and the frequencies and other operators are obtained in a data-driven fashion as mentioned in section III. Figure 4 shows the time evolution of the second POD mode for different time horizons, where 'T' is the time horizon used for training. The time evolution of this POD mode appears to be narrow-banded; although not shown here, the time evolution of the first POD mode is similar to it, but with a phase shift. Similarly, the evolution of third POD mode is similar to the fourth one with a phase shift and is also narrow-banded. Figure 4 (a) shows the comparison between the ground truth i.e., POD coefficients computed from DNS

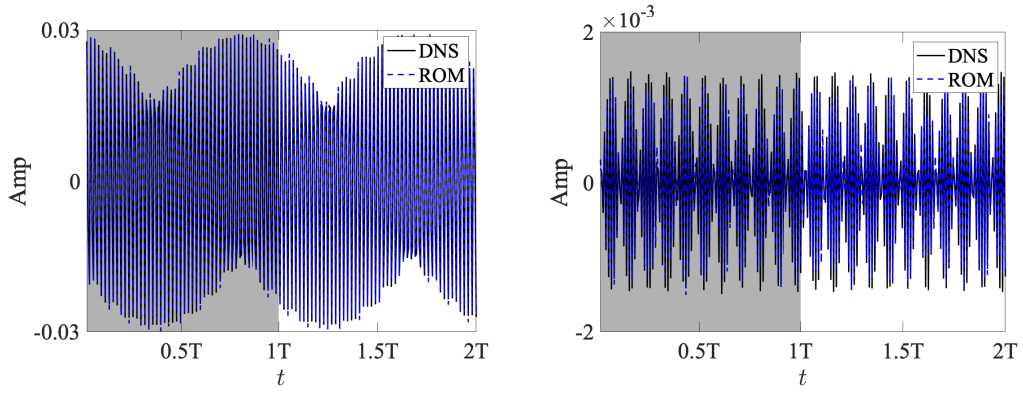

(a) 20^{th} POD mode (b) 28^{th} POD mode

Fig. 5 Comparison of the truncated modes estimated via the proposed trigonometric closure model and the DNS ground truth. The higher-order modes are derived from the leading modes via Eq. (6).

in solid black line and the ROM predictions in dashed blue line. The predictions are in very good agreement with the DNS in the training horizon as well as beyond it. Figure 4(b) shows the ROM and the DMD marched forward for $500T$. The 4 mode DMD model without a closure (shown as DMD) shows an exponential decay in the amplitude while the amplitude of the ROM remains constant. This is because the 4 mode DMD model does not account for the interaction between the leading and truncated modes. In contrast, this interaction is accounted for and the trajectories are corrected when using the 4 mode DMD with trigonometric closure (shown as ROM). The closure modeling not only corrects the state trajectories but also facilitates estimation of the higher-order modes. Figure 5 shows the estimates for the 20^{th} and 28^{th} mode to compare with the DNS ground truth. As before, the estimates closely match the DNS within and beyond the training horizon. These modes appear to have multiple frequencies. For example, the 20^{th} mode (see figure 5(a)) has a high frequency signal embeded inside a low frequency one. Similarly, the 28^{th} mode (see figure 5(b)) also has a multiple frequencies. Note that the underlying model is 4 dimensional with a trigonometric closure. Therefore, the higher-order modes are represented as a function of the leading first 4 POD modes via the closure model in Eq. (6). As discussed in subsection II.B we use the property of the sine and cosine functions in generating higher and broad-banded frequency content from low frequency leading POD modes. When using this closure model, the extent to which the truncated modes can be represented reasonably well can be tuned by the number of frequencies f_{ij} to use. Here, we use 8 frequencies per mode (32 in total) and were able to approximate about 30 truncated modes. Using the two-step training approach discussed in section III.A the model approximates the frequency of the target signal and calibrates it, thereby approximating a wide range of truncated modes.

1. Accuracy of the reconstructed flow fields

Figure 6 shows the reconstructed flow field from DMD and the ROM against the DNS ground truth over the last snapshot of the testing dataset. Although the 4-mode DMD model captures the location of the vortices, they appear smeared out. However, the reconstructed flow fields from the ROM are a closer match to the DNS and the vortices are more distinct. An integrated error metric is computed to assess the accuracy of the reconstructed flow fields. This error metric is given by

$$\epsilon = \frac{\|\mathbf{u} - \hat{\mathbf{u}}\|_{\text{Fro}}}{\|\mathbf{u}\|_{\text{Fro}}}, \tag{16}$$

where $\mathbf{u} = \begin{bmatrix} u & v \end{bmatrix}^{\text{T}}$ with u and v denoting the streamwise and vertical velocity fluctuations. The variable with a hat $\hat{(\cdot)}$ is for the ROM predictions and the unhatted variable is for the DNS gound truth. The accuracy (α) is given by

$$\alpha = (1 - \epsilon) \times 100. \tag{17}$$

The accuracy of the model is computed for both the DMD and the ROM are shown in Table 2. The accuracy of the

reconstructed flow field is increased by about 15% when using the trigonometric closure. These results underscore the current approach's capability to build low-order models without sacrificing accuracy.

Table 2 Prediction error for DMD and ROM over training and testing datasets.

	Train	Test
DMD	87.0%	86.9 %
ROM	99.9%	99.9 %

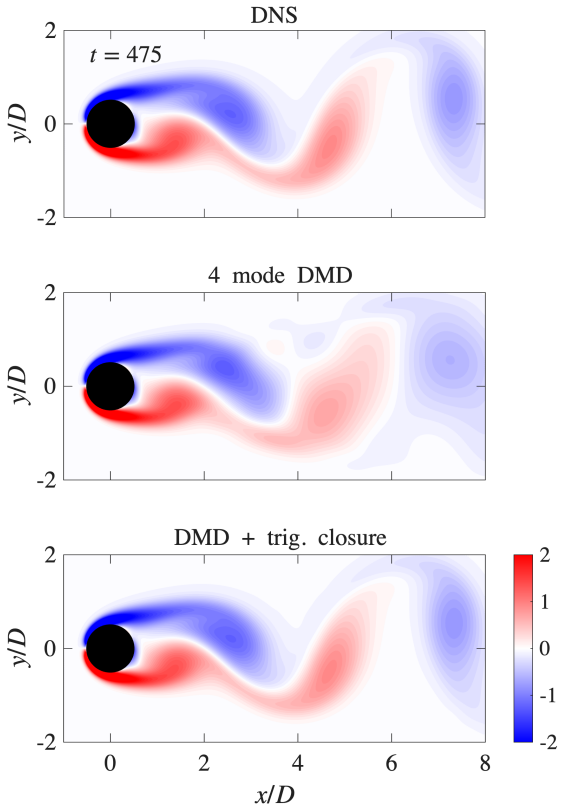

Fig. 6 Vorticity contours from the flow fields reconstructed for a 4-mode DMD and the ROM to compare with the DNS over the last snapshot of the testing dataset. The vortices appear to be smeared out for DMD whereas they are more distinct when using the closure model.

2. Long-time behaviour

Figure 7 shows the long-time behavior when the ROM is marched forwards in time for 500 training time horizons for different values of the regularization parameter λ. The operator $\overline{\mathbf{\Phi}}$ is computed via ridge regression as

$$\overline{\mathbf{\Phi}} = \arg\min_{\mathbf{Y}} \| (\tilde{\mathbf{x}} - \Phi\hat{\mathbf{x}}) - \mathbf{Y}C(\hat{\mathbf{x}})\|^2 + \lambda\|\mathbf{Y}\|^2. \tag{18}$$

Here $C(\hat{\mathbf{x}})$ represents the closure terms, it is $C(\hat{\mathbf{x}}) = (\hat{\mathbf{x}} \otimes \hat{\mathbf{x}})$ for a quadratic closure and is the vector of sine-cosine pairs of different frequencies for the trigonometric closure given by $\tau(f_{ij}, \hat{\mathbf{x}})$ in Eq. 6.

For a quadratic closure, when $\lambda = 19$ (see figure 7(a)), the amplitude appears to be constant until $375T$ but the solution quickly diverges. Increasing this value to $\lambda = 20$ results in the amplitude decay as shown in figure 7(b). Therefore, a very careful tuning of the regularization parameter is necessary for the solution to be bounded or non-zero

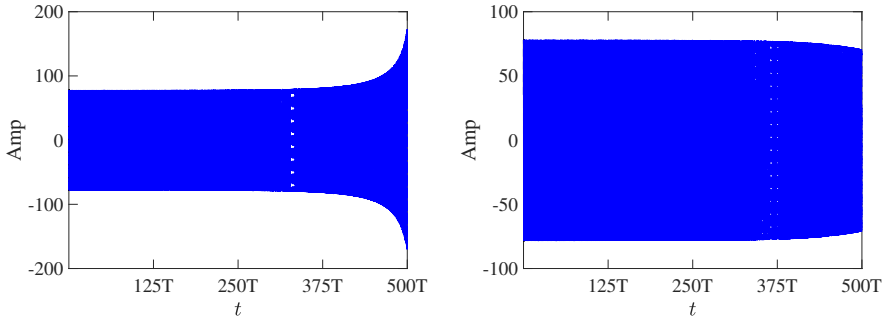

(a) $(Quad.)\lambda = 19$ (b) $(Quad.)\lambda = 20$

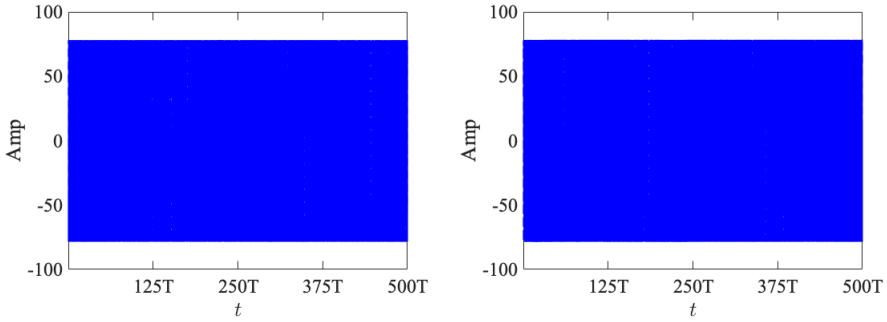

(c) $(Trig.)\lambda = 10^{-2}$ (d) $(Trig.)\lambda = 10^{2}$

Fig. 7 Long-time behavior of the solution after time marching the ROM for $500T$. When using quadratic closure (see subplots (a) and (b)), the amplitude appears to remain constant until $375T$. However, even with a small change in the hyperparameter λ in the ridge regression, the solution's nature changes from blowing up to decaying beyond $375T$. On the other hand, the amplitude remains bounded when using trigonometric closure even though there is 4 order of magnitude change in λ(see subplots (c) and (d)).

within the time horizon we need. On the other hand, when using a trigonometric closure, the results do not appear to change much even with a significant change in λ. Figure 7(c) shows the solution for $\lambda = 10^{-2}$. When λ is increased to 10^2, the amplitude still remains constant and is long-time bounded. For other test cases, not shown here, tuning λ can increase the accuracy of the model but the solution never blows up as long as the liner operator is stable.

B. Academic Example: Two-Dimensional Limit Cycle

We demonstrate the trapping region analysis in Section III.B for an academic example constructed from the previously discussed cylinder wake case. First, we use the proposed data-driven modeling framework to obtain a two-state model of the form (7) with two frequencies per state for the trigonometric closures. We then artificially dampen the eigenvalues of the linear operator* as

$$\hat{\mathbf{A}} = \hat{\mathbf{A}}_{cw} - 10^{-2}\mathbf{I} \tag{19}$$

where $\hat{\mathbf{A}}_{cw}$ is the linear operator obtained via DMD for the cylinder wake. The resulting model is then time integrated for several, randomly chosen initial conditions and the trajectories are shown in Fig. 8(a), where the starting point for each trajectory is shown by a filled black circle. All these trajectories converge to a limit cycle (i.e., an attractor) indicating a bounded response of the model.

As mentioned in Section III.B, the optimization in Eq. (15) is non-convex due to the bilinear term $\lambda_1\mathbf{P}$. Therefore, we grid over λ_1 to reformulate (15) as

$$\begin{aligned} &\max_{\mathbf{P}>0,\lambda_2,\gamma} \ \gamma \\ &\text{subject to (11), } \mathbf{P} \geq \gamma\mathbf{I} \end{aligned} \tag{20}$$

where $\lambda_1 \in \Lambda_1$ with $\Lambda_1 \in (0, 1)$ as the specified grid. Note that the above optimization in (20) is a semi-definite program or SDP (convex) and we solve this SDP to obtain γ for $\lambda_1 \in \Lambda_1$. Then, the optimal trapping region radius is $R^\star = 1/\sqrt{(}\gamma^\star)$ where $\gamma^\star = \max_{\lambda_1\in\Lambda_1}\gamma$. Variation of the trapping region radius for $\lambda_1 \in \Lambda_1$ for this example is illustrated in Fig. 8(b). The optimal (minimum) radius of the trapping region obtained here is approximately 26.65 and corresponds to $\lambda_1 = 0.0098$. However, the limit cycle shown Fig. 8(a) can be inscribed in a circle of radius approximately equal to 3. Thus, the trapping region radius obtained through the analysis here is roughly one order of magnitude higher but it can provide a quick estimate on the ultimate bound of the responses for a model that we synthesize. The generalized energy associated with the trajectories in Fig. 8(a) are depicted in Fig. 8(c). For the results in Fig. 8(c), we have utilized the generalized energy matrix $\mathbf{P}$ associated with the minimum trapping radius (which is obtained by solving the optimization in (20) for $\lambda_1 = 0.0098$).

The energy monotonically decreases outside of the trapping region and oscillates about a fixed value as the trajectories converge onto the limit cycle.

V. Conclusions and future work

In this work, we proposed a trigonometric closure using sine-cosine pairs of different frequencies that can be integrated with a low-order linear model as a non-linear forcing term. The utility of using a trigonometric closure model is three fold:

- *Approximation of manifolds*: Because many high-dimensional physical systems evolve on a low-dimensional manifold, accurately approximating this manifold can improve predictive fidelity of a low-order model. Using sine-cosine pairs of multiple frequencies can be interpreted as approximating this low-dimensional complex manifold using a Fourier series with limited terms. The number of frequencies can be a hyperparameter to improve the approximation.
- *Expressive basis*: Choosing sine-cosine pairs as the basis functions of a closure model forms an expressive basis. It has the ability to generate higher and broadbanded frequency output signals from a narrow-banded input. We demonstrated this property for the test case of a cylinder wake where the narrow-banded leading modes were mapped to broadbanded and high frequency higher-order truncated modes reasonable well.
- *Boundedness guarantees*: The ROM is guaranteed to be long-time bounded when the linear operator is stable, i.e., when it has spectral radius strictly less than 1. We showed that in such a case, the ROM admits a trapping region whereby the ROM states are guaranteed to converge to an ellipsoid in the state space. In addition, we formulated a

*This is done for illustration purposes as well as satisfying Assumption 1 required for the trapping region analysis.

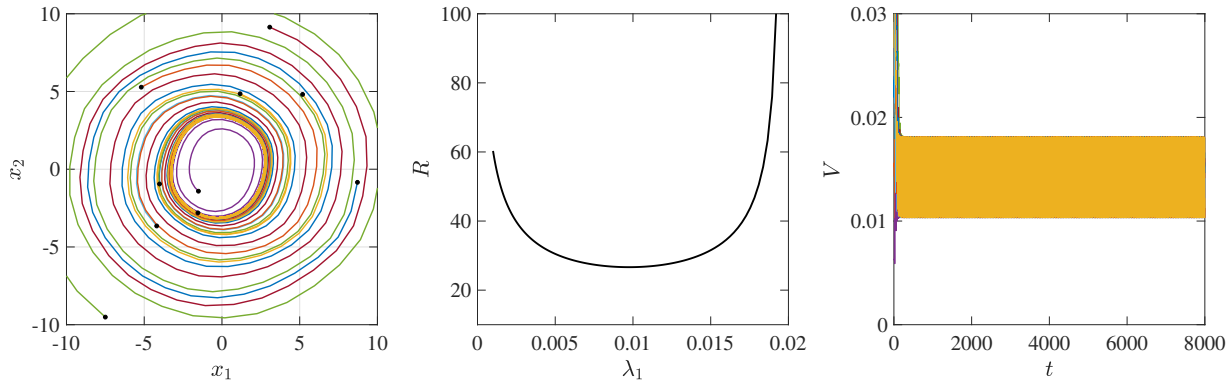

Fig. 8 System synthesized from a 2 state 2 frequency per mode cylinder wake model: (a) Time history of trajectories evolving from randomly chosen initial conditions which are indicated by black filled circles; (b) Trapping region radius as a function of λ_1; (c) Time evolution of generalized energy $V = \mathbf{x}^{\mathrm{T}}\mathbf{P}\mathbf{x}$ for the trajectories in (a). Here, P is computed using the optimization in Eq. (20) for $\lambda_1 = 0.0098$, which corresponds to the minimum radius in (b).

convex optimization—more specifically, a semi-definite program—to compute the smallest norm-ball inscribing the ellipsoid. Radius of the norm-ball serves as an estimate of the ultimate bound for the trajectories of the ROM with trigonometric closures.

We demonstrated these features of the proposed trigonometric closure model on a transient cylinder wake and a periodic cylinder wake. Results show that this closure model improves the predictive fidelity and makes the resulting ROM long-time bounded.

The proposed trigonometric closure is a purely data-driven model and the frequencies and the operators are obtained via optimization over the training snapshots. Although we use DMD to obtain the linear operator for the examples included in this paper, other techniques can also be used. Therefore, simultaneously computing a stable linear operator and a trigonometric closure model by minimizing the prediction error subject to appropriate constraints is one possible future direction. Many physical systems are governed by quadratic nonlinear dynamics including the Navier-Stokes equations, Lorenz system, etc., and the quadratic nonlinearity in the ROM would play a crucial role in capturing the rich dynamics displayed by these systems. Therefore, another potential line of work could be to integrate this closure model to a linear-quadratic model where the quadratic nonlinearity may satisfy the lossless property [20, 21]. Overall, the framework in this paper should lay the foundation for future studies on employing the proposed trigonometric closure as a correction and lifting term for low-order models geared towards various engineering applications.

VI. Acknowledgments

This material is based upon work supported by the Air Force Office of Scientific Research under Award Number FA9550-21-1-0434. The authors are thankful to Shih-Chi Liao for helpful discussions on the trapping region analysis.

References

[1] Holmes, P., Turbulence, coherent structures, dynamical systems and symmetry, Cambridge university press, 2012.

[2] Meilă, M., and Zhang, H., "Manifold learning: What, how, and why," Annual Review of Statistics and Its Application, Vol. 11, No. 1, 2024, pp. 393–417.

[3] Diaz, A. N., Choi, Y., and Heinkenschloss, M., "A fast and accurate domain decomposition nonlinear manifold reduced order model," Computer Methods in Applied Mechanics and Engineering, Vol. 425, 2024, p. 116943.

[4] Sahyoun, S., and Djouadi, S., "Local proper orthogonal decomposition based on space vectors clustering," 3rd International Conference on Systems and Control, IEEE, 2013, pp. 665–670.

[5] Wu, T., Wilson, D., and Djouadi, S., "Manifold Clustering Based Nonlinear Model Reduction with Application to Nonlinear Convection," 2024 IEEE 63rd Conference on Decision and Control (CDC), IEEE, 2024, pp. 2697–2702.

[6] Lee, K., and Carlberg, K. T., "Model reduction of dynamical systems on nonlinear manifolds using deep convolutional autoencoders," Journal of Computational Physics, Vol. 404, 2020, p. 108973.

[7] Kim, Y., Choi, Y., Widemann, D., and Zohdi, T., "Efficient nonlinear manifold reduced order model," arXiv preprint arXiv:2011.07727, 2020.

[8] Diaz, A. N., Choi, Y., and Heinkenschloss, M., "Nonlinear-manifold reduced order models with domain decomposition," arXiv preprint arXiv:2312.00713, 2023.

[9] Rutzmoser, J. B., Rixen, D. J., Tiso, P., and Jain, S., "Generalization of quadratic manifolds for reduced order modeling of nonlinear structural dynamics," Computers & Structures, Vol. 192, 2017, pp. 196–209.

[10] Barnett, J., and Farhat, C., "Quadratic approximation manifold for mitigating the Kolmogorov barrier in nonlinear projection-based model order reduction," Journal of Computational Physics, Vol. 464, 2022, p. 111348.

[11] Geelen, R., Wright, S., and Willcox, K., "Operator inference for non-intrusive model reduction with quadratic manifolds," Computer Methods in Applied Mechanics and Engineering, Vol. 403, 2023, p. 115717.

[12] Geelen, R., Balzano, L., Wright, S., and Willcox, K., "Learning physics-based reduced-order models from data using nonlinear manifolds," Chaos: An Interdisciplinary Journal of Nonlinear Science, Vol. 34, No. 3, 2024.

[13] Schlegel, M., and Noack, B. R., "On long-term boundedness of Galerkin models," Journal of Fluid Mechanics, Vol. 765, 2015, pp. 325–352.

[14] Erichson, N. B., Muehlebach, M., and Mahoney, M. W., "Physics-informed autoencoders for Lyapunov-stable fluid flow prediction," arXiv preprint arXiv:1905.10866, 2019.

[15] Kaptanoglu, A. A., Callaham, J. L., Aravkin, A., Hansen, C. J., and Brunton, S. L., "Promoting global stability in data-driven models of quadratic nonlinear dynamics," Physical Review Fluids, Vol. 6, No. 9, 2021, p. 094401.

[16] Goyal, P., Duff, I. P., and Benner, P., "Guaranteed stable quadratic models and their applications in SINDy and operator inference," arXiv preprint arXiv:2308.13819, 2023.

[17] Heide, A. L., Liao, S.-C., Castiblanco-Ballesteros, S., Jacobs, G., Seiler, P., and Hemati, M., "Low-order nonlinear aerodynamics models from data with boundedness guarantees," APS Division of Fluid Dynamics Meeting Abstracts, 2024, pp. L15–011.

[18] Khalil, H. K., Nonlinear systems, Vol. 3, Prentice hall Upper Saddle River, NJ, 2002.

[19] Slotine, J.-J. E., and Li, W., Applied nonlinear control, Vol. 199, Prentice hall Englewood Cliffs, NJ, 1991.

[20] Liao, S.-C., Leonid Heide, A., Hemati, M. S., and Seiler, P. J., "A convex optimization approach to compute trapping regions for lossless quadratic systems," International Journal of Robust and Nonlinear Control, Vol. 35, No. 6, 2025, pp. 2425–2436.

[21] Peng, M., Kaptanoglu, A., Hansen, C., Stevens-Haas, J., Manohar, K., and Brunton, S. L., "Local stability guarantees for data-driven quadratically nonlinear models," , 2024. URL https://arxiv.org/abs/2403.00324.

[22] Noack, B. R., Afanasiev, K., Morzyński, M., Tadmor, G., and Thiele, F., "A hierarchy of low-dimensional models for the transient and post-transient cylinder wake," Journal of Fluid Mechanics, Vol. 497, 2003, pp. 335–363.

[23] Kalur, A., Mortimer, P., Sirohi, J., Geelen, R., and Willcox, K. E., "Data-driven closures for the dynamic mode decomposition using quadratic manifolds," AIAA AVIATION 2023 Forum, 2023, p. 4352.

[24] Schmid, P. J., "Dynamic mode decomposition of numerical and experimental data," Journal of fluid mechanics, Vol. 656, 2010, pp. 5–28.

[25] Ahmed, S. E., Pawar, S., San, O., Rasheed, A., Iliescu, T., and Noack, B. R., "On closures for reduced order models—A spectrum of first-principle to machine-learned avenues," Physics of Fluids, Vol. 33, No. 9, 2021.

[26] Kalur, A., Mushtaq, T., Seiler, P., and Hemati, M. S., "Estimating regions of attraction for transitional flows using quadratic constraints," IEEE Control Systems Letters, Vol. 6, 2021, pp. 482–487.

[27] Liao, S.-C., Hemati, M. S., and Seiler, P., "Quadratic constraints for local stability analysis of quadratic systems," 2022 IEEE 61st Conference on Decision and Control (CDC), IEEE, 2022, pp. 7053–7058.

[28] Caverly, R. J., and Forbes, J. R., "LMI properties and applications in systems, stability, and control theory," arXiv preprint arXiv:1903.08599, 2019.

[29] Boyd, S., El Ghaoui, L., Feron, E., and Balakrishnan, V., Linear matrix inequalities in system and control theory, SIAM, 1994.

[30] Taira, K., and Colonius, T., "The immersed boundary method: a projection approach," Journal of Computational Physics, Vol. 225, No. 2, 2007, pp. 2118–2137.

[31] Colonius, T., and Taira, K., "A fast immersed boundary method using a nullspace approach and multi-domain far-field boundary conditions," Computer Methods in Applied Mechanics and Engineering, Vol. 197, No. 25-28, 2008, pp. 2131–2146.

[32] Rowley, C., "Immersed Boundary Projection Method (IBPM)," , Accessed in October, 2024. URL `https://github.com/cwrowley/ibpm.git`.

A. Alternative Characterization of Trapping Region

The following result provides an alternative characterization of the trapping region for system (7) in terms of a norm ball.

Theorem 2 *Under Assumption 1, system* (7) *admits a trapping region* $\{\hat{\mathbf{x}} \in \mathbb{R}^r : \hat{\mathbf{x}}^{\mathrm{T}}\hat{\mathbf{x}} \leq R^2\}$ *whose radius* R *is given by*

$$R = \frac{ab\|\mathbf{P}\|}{|\lambda_m|} + \frac{b}{|\lambda_m|}\left(\sqrt{|\lambda_m|}\|\mathbf{P}\| + a^2\|\mathbf{P}\|^2\right)^{1/2} \tag{21}$$

where $\mathbf{P} > 0$ *such that* $\hat{\mathbf{A}}^{\mathrm{T}}\mathbf{P}\hat{\mathbf{A}} - \mathbf{P} < 0$ *and* $\lambda_m := \lambda_{\max}\left(\hat{\mathbf{A}}^{\mathrm{T}}\mathbf{P}\hat{\mathbf{A}} - \mathbf{P}\right)$ *with* $a := \|\hat{\mathbf{A}}\|$, $b := \|\hat{\mathbf{B}}\|$.

Proof: Consider the generalized energy $V(\hat{\mathbf{x}}(k)) := \frac{1}{2}\hat{\mathbf{x}}^{\mathrm{T}}(k)\mathbf{P}\hat{\mathbf{x}}(k)$ with a $\mathbf{P} > 0$ and set $\tau(k) := \tau(f_{ij}, \hat{\mathbf{x}}(k))$ to simplify notations. Then, the change in energy is given by $V(\hat{\mathbf{x}}(k+1)) - V(\hat{\mathbf{x}}(k)) = \frac{1}{2}\hat{\mathbf{x}}^{\mathrm{T}}(k+1)\mathbf{P}\hat{\mathbf{x}}(k+1) - \frac{1}{2}\hat{\mathbf{x}}^{\mathrm{T}}(k)\mathbf{P}\hat{\mathbf{x}}(k)$, which can be expressed as

$$\begin{aligned}
&V(\hat{\mathbf{x}}(k+1)) - V(\hat{\mathbf{x}}(k)) \\
&= \frac{1}{2}\hat{\mathbf{x}}^{\mathrm{T}}(k)\left(\hat{\mathbf{A}}^{\mathrm{T}}\mathbf{P}\hat{\mathbf{A}} - \mathbf{P}\right)\hat{\mathbf{x}}(k) + \frac{1}{2}\hat{\mathbf{x}}^{\mathrm{T}}(k)\hat{\mathbf{A}}^{\mathrm{T}}\mathbf{P}\hat{\mathbf{B}}\tau(k) + \frac{1}{2}\tau^{\mathrm{T}}(k)\hat{\mathbf{B}}^{\mathrm{T}}\mathbf{P}\hat{\mathbf{A}}\hat{\mathbf{x}}(k) + \frac{1}{2}\tau^{\mathrm{T}}(k)\hat{\mathbf{B}}^{\mathrm{T}}\mathbf{P}\hat{\mathbf{B}}\tau(k).
\end{aligned}$$

Applying the Cauchy–Schwarz inequality to the right hand side of the above and using Assumption 1 yields an upper bound on the change in energy as

$$V(\hat{\mathbf{x}}(k+1)) - V(\hat{\mathbf{x}}(k)) \leq \frac{1}{2}\lambda_m\|\hat{\mathbf{x}}(k)\|^2 + ab\|\mathbf{P}\|\|\hat{\mathbf{x}}(k)\| + \frac{1}{2}b^2\|\mathbf{P}\| \tag{22}$$

where $\lambda_m := \lambda_{\max}\left(\hat{\mathbf{A}}^{\mathrm{T}}\mathbf{P}\hat{\mathbf{A}} - \mathbf{P}\right)$, $a := \|\hat{\mathbf{A}}\|$, $b := \|\hat{\mathbf{B}}\|$. Since $\hat{\mathbf{A}}$ is stable under Assumption 1, there exists $\mathbf{P} > 0$ such that $\hat{\mathbf{A}}^{\mathrm{T}}\mathbf{P}\hat{\mathbf{A}} - \mathbf{P} < 0$. Thus, choosing such a $\mathbf{P}$ makes $\lambda_m < 0$ and the upper bound in (22) becomes negative for

$$\|\hat{\mathbf{x}}(k)\| > \frac{ab\|\mathbf{P}\|}{|\lambda_m|} + \frac{b}{|\lambda_m|}\left(\sqrt{|\lambda_m|}\|\mathbf{P}\| + a^2\|\mathbf{P}\|^2\right)^{1/2}.$$

Therefore, the set $\{\hat{\mathbf{x}} \in \mathbb{R}^r : \hat{\mathbf{x}}^{\mathrm{T}}\hat{\mathbf{x}} \leq R^2\}$ with R as in Eq. (21) is forward invariant with respect to the dynamics (7), which makes it a trapping region. This completes the proof. □

The radius R in Eq. (21) grows monotonically with $\|\mathbf{P}\|$ and the optimal (i.e., minimum) radius would correspond to a minimization in $\|\mathbf{P}\|$ subject to the associated constraints. This can be posed as the following optimization:

$$\min_{\mathbf{P}} \|\mathbf{P}\| \tag{23}$$

$$\mathbf{P} > 0, \hat{\mathbf{A}}^{\mathrm{T}}\mathbf{P}\hat{\mathbf{A}} - \mathbf{P} < 0 \tag{24}$$

which can be equivalently expressed as

$$\min_{s,\mathbf{P}} s \tag{25}$$

$$\begin{bmatrix} s\mathbf{I} & \mathbf{P} \\ \mathbf{P} & s\mathbf{I} \end{bmatrix} \geq 0, \tag{26}$$

$$\mathbf{P} > 0, \hat{\mathbf{A}}^{\mathrm{T}}\mathbf{P}\hat{\mathbf{A}} - \mathbf{P} \leq -|\lambda_m|\mathbf{I} \tag{27}$$

with a grid for $|\lambda_m|$. Thus, the optimal radius would correspond to the minimum of the optimal solutions obtained from solving the above optimization (which is an SDP in variables $s, \mathbf{P}$) over the specified $|\lambda_m|$ grid.